Multi-Megahertz OCT: High quality 3D imaging at 20 million A-scans and 4.5 GVoxels per second

Wolfgang Wieser, Benjamin R. Biedermann, Thomas Klein, Christoph M. Eigenwillig and Robert Huber*

Lehrstuhl für BioMolekulare Optik, Fakultät für Physik, Ludwig-Maximilians-Universität München,Oettingenstr. 67, 80538 Munich, Germany
**Robert.Huber@LMU.DE*

Abstract: We present ultra high speed optical coherence tomography (OCT) with multi-megahertz line rates and investigate the achievable image quality. The presented system is a swept source OCT setup using a Fourier domain mode locked (FDML) laser. Three different FDML-based swept laser sources with sweep rates of 1, 2.6 and 5.2MHz are compared. Imaging with 4 spots in parallel quadruples the effective speed, enabling depth scan rates as high as 20.8 million lines per second. Each setup provides at least 98dB sensitivity and ~10µm resolution in tissue. High quality 2D and 3D imaging of biological samples is demonstrated at full scan speed. A discussion about how to best specify OCT imaging speed is included. The connection between voxel rate, line rate, frame rate and hardware performance of the OCT setup such as sample rate, analog bandwidth, coherence length, acquisition dead-time and scanner duty cycle is provided. Finally, suitable averaging protocols to further increase image quality are discussed.

©2010 Optical Society of America

OCIS codes: (110.4500) Imaging systems: Optical coherence tomography; (140.3600) Lasers, tunable; (110.6880) Three-dimensional image acquisition; (170.4500) Optical coherence tomography.

References and links

1. D. Huang, E. A. Swanson, C. P. Lin, J. S. Schuman, W. G. Stinson, W. Chang, M. R. Hee, T. Flotte, K. Gregory, C. A. Puliafito, and J. G. Fujimoto, "Optical coherence tomography," Science **254**(5035), 1178–1181 (1991).
2. A. F. Fercher, C. K. Hitzenberger, G. Kamp, and S. Y. Elzaiat, "Measurement of intraocular distances by backscattering spectral interferometry," Opt. Commun. **117**(1-2), 43–48 (1995).
3. G. Häusler, and M. W. Lindner, "'Coherence radar' and 'spectral radar'-new tools for dermatological diagnosis," J. Biomed. Opt. **3**(1), 21–31 (1998).
4. M. A. Choma, M. V. Sarunic, C. H. Yang, and J. A. Izatt, "Sensitivity advantage of swept source and Fourier domain optical coherence tomography," Opt. Express **11**(18), 2183–2189 (2003).
5. J. F. de Boer, B. Cense, B. H. Park, M. C. Pierce, G. J. Tearney, and B. E. Bouma, "Improved signal-to-noise ratio in spectral-domain compared with time-domain optical coherence tomography," Opt. Lett. **28**(21), 2067–2069 (2003).
6. R. Leitgeb, C. K. Hitzenberger, and A. F. Fercher, "Performance of fourier domain vs. time domain optical coherence tomography," Opt. Express **11**(8), 889–894 (2003).
7. S. H. Yun, G. J. Tearney, J. F. de Boer, N. Iftimia, and B. E. Bouma, "High-speed optical frequency-domain imaging," Opt. Express **11**(22), 2953–2963 (2003).
8. W. Y. Oh, S. H. Yun, B. J. Vakoc, G. J. Tearney, and B. E. Bouma, "Ultrahigh-speed optical frequency domain imaging and application to laser ablation monitoring," Appl. Phys. Lett. **88**(10), 103902 (2006).
9. R. Huber, M. Wojtkowski, and J. G. Fujimoto, "Fourier Domain Mode Locking (FDML): A new laser operating regime and applications for optical coherence tomography," Opt. Express **14**(8), 3225–3237 (2006).
10. R. Huber, D. C. Adler, and J. G. Fujimoto, "Buffered Fourier domain mode locking: Unidirectional swept laser sources for optical coherence tomography imaging at 370,000 lines/s," Opt. Lett. **31**(20), 2975–2977 (2006).
11. S. H. Yun, G. J. Tearney, B. J. Vakoc, M. Shishkov, W. Y. Oh, A. E. Desjardins, M. J. Suter, R. C. Chan, J. A. Evans, I. K. Jang, N. S. Nishioka, J. F. de Boer, and B. E. Bouma, "Comprehensive volumetric optical microscopy in vivo," Nat. Med. **12**(12), 1429–1433 (2006).
12. D. C. Adler, Y. Chen, R. Huber, J. Schmitt, J. Connolly, and J. G. Fujimoto, "Three-dimensional endomicroscopy using optical coherence tomography," Nat. Photonics **1**(12), 709–716 (2007).

#126756 - $15.00 USD Received 9 Apr 2010; revised 4 Jun 2010; accepted 15 Jun 2010; published 30 Jun 2010
(C) 2010 OSA

13. R. Huber, D. C. Adler, V. J. Srinivasan, and J. G. Fujimoto, "Fourier domain mode locking at 1050 nm for ultra-high-speed optical coherence tomography of the human retina at 236,000 axial scans per second," Opt. Lett. **32**(14), 2049–2051 (2007).
14. B. Potsaid, I. Gorczynska, V. J. Srinivasan, Y. L. Chen, J. Jiang, A. Cable, and J. G. Fujimoto, "Ultrahigh speed spectral / Fourier domain OCT ophthalmic imaging at 70,000 to 312,500 axial scans per second," Opt. Express **16**(19), 15149–15169 (2008).
15. N. A. Nassif, B. Cense, B. H. Park, M. C. Pierce, S. H. Yun, B. E. Bouma, G. J. Tearney, T. C. Chen, and J. F. de Boer, "In vivo high-resolution video-rate spectral-domain optical coherence tomography of the human retina and optic nerve," Opt. Express **12**(3), 367–376 (2004).
16. Y. Yasuno, V. D. Madjarova, S. Makita, M. Akiba, A. Morosawa, C. Chong, T. Sakai, K. P. Chan, M. Itoh, and T. Yatagai, "Three-dimensional and high-speed swept-source optical coherence tomography for in vivo investigation of human anterior eye segments," Opt. Express **13**(26), 10652–10664 (2005).
17. R. Huber, M. Wojtkowski, J. G. Fujimoto, J. Y. Jiang, and A. E. Cable, "Three-dimensional and C-mode OCT imaging with a compact, frequency swept laser source at 1300 nm," Opt. Express **13**(26), 10523–10538 (2005).
18. S. L. Jiao, R. Knighton, X. R. Huang, G. Gregori, and C. A. Puliafito, "Simultaneous acquisition of sectional and fundus ophthalmic images with spectral-domain optical coherence tomography," Opt. Express **13**(2), 444–452 (2005).
19. S. W. Huang, A. D. Aguirre, R. A. Huber, D. C. Adler, and J. G. Fujimoto, "Swept source optical coherence microscopy using a Fourier domain mode-locked laser," Opt. Express **15**(10), 6210–6217 (2007).
20. W. Y. Oh, S. H. Yun, G. J. Tearney, and B. E. Bouma, "115 kHz tuning repetition rate ultrahigh-speed wavelength-swept semiconductor laser," Opt. Lett. **30**(23), 3159–3161 (2005).
21. M. W. Jenkins, D. C. Adler, M. Gargesha, R. Huber, F. Rothenberg, J. Belding, M. Watanabe, D. L. Wilson, J. G. Fujimoto, and A. M. Rollins, "Ultrahigh-speed optical coherence tomography imaging and visualization of the embryonic avian heart using a buffered Fourier Domain Mode Locked laser," Opt. Express **15**(10), 6251–6267 (2007).
22. V. J. Srinivasan, D. C. Adler, Y. L. Chen, I. Gorczynska, R. Huber, J. S. Duker, J. S. Schuman, and J. G. Fujimoto, "Ultrahigh-speed optical coherence tomography for three-dimensional and en face imaging of the retina and optic nerve head," Invest. Ophthalmol. Vis. Sci. **49**(11), 5103–5110 (2008).
23. A. Szkulmowska, M. Szkulmowski, D. Szlag, A. Kowalczyk, and M. Wojtkowski, "Three-dimensional quantitative imaging of retinal and choroidal blood flow velocity using joint Spectral and Time domain Optical Coherence Tomography," Opt. Express **17**(13), 10584–10598 (2009).
24. D. Choi, H. Hiro-Oka, H. Furukawa, R. Yoshimura, M. Nakanishi, K. Shimizu, and K. Ohbayashi, "Fourier domain optical coherence tomography using optical demultiplexers imaging at 60,000,000 lines/s," Opt. Lett. **33**(12), 1318–1320 (2008).
25. S. Moon, and D. Y. Kim, "Ultra-high-speed optical coherence tomography with a stretched pulse supercontinuum source," Opt. Express **14**(24), 11575–11584 (2006).
26. K. Goda, D. R. Solli, and B. Jalali, "Real-time optical reflectometry enabled by amplified dispersive Fourier transformation," Appl. Phys. Lett. **93**(3), 031106 (2008).
27. B. R. Biedermann, W. Wieser, C. M. Eigenwillig, T. Klein, and R. Huber, "Dispersion, coherence and noise of Fourier domain mode locked lasers," Opt. Express **17**(12), 9947–9961 (2009).
28. B. Golubovic, B. E. Bouma, G. J. Tearney, and J. G. Fujimoto, "Optical frequency-domain reflectometry using rapid wavelength tuning of a Cr4+:forsterite laser," Opt. Lett. **22**(22), 1704–1706 (1997).
29. R. Huber, M. Wojtkowski, K. Taira, J. G. Fujimoto, and K. Hsu, "Amplified, frequency swept lasers for frequency domain reflectometry and OCT imaging: design and scaling principles," Opt. Express **13**(9), 3513–3528 (2005).
30. T. Bajraszewski, M. Wojtkowski, M. Szkulmowski, A. Szkulmowska, R. Huber, and A. Kowalczyk, "Improved spectral optical coherence tomography using optical frequency comb," Opt. Express **16**(6), 4163–4176 (2008).
31. J. A. Izatt, M. R. Hee, G. M. Owen, E. A. Swanson, and J. G. Fujimoto, "Optical coherence microscopy in scattering media," Opt. Lett. **19**(8), 590–592 (1994).
32. A. G. Podoleanu, "Fiber optics, from sensing to non-invasive high-resolution medical imaging," J. Lightwave Technol. **28**(4), 624–640 (2010).
33. B. R. Biedermann, W. Wieser, C. M. Eigenwillig, and R. Huber, "Recent developments in Fourier domain mode locked lasers for optical coherence tomography: imaging at 1310 nm vs. 1550 nm wavelength," J Biophotonics **2**(6-7), 357–363 (2009).
34. S. H. Yun, G. J. Tearney, J. F. de Boer, and B. E. Bouma, "Removing the depth-degeneracy in optical frequency domain imaging with frequency shifting," Opt. Express **12**(20), 4822–4828 (2004).
35. A. M. Davis, M. A. Choma, and J. A. Izatt, "Heterodyne swept-source optical coherence tomography for complete complex conjugate ambiguity removal," J. Biomed. Opt. **10**(6), 064005 (2005).
36. T. Klein, W. Wieser, B. R. Biedermann, C. M. Eigenwillig, G. Palte, and R. Huber, "Raman-pumped Fourier-domain mode-locked laser: analysis of operation and application for optical coherence tomography," Opt. Lett. **33**(23), 2815–2817 (2008).
37. C. Jirauschek, B. Biedermann, and R. Huber, "A theoretical description of Fourier domain mode locked lasers," Opt. Express **17**(26), 24013–24019 (2009).
38. G. Y. Liu, A. Mariampillai, B. A. Standish, N. R. Munce, X. J. Gu, and I. A. Vitkin, "High power wavelength linearly swept mode locked fiber laser for OCT imaging," Opt. Express **16**(18), 14095–14105 (2008).

#126756 - $15.00 USD Received 9 Apr 2010; revised 4 Jun 2010; accepted 15 Jun 2010; published 30 Jun 2010
(C) 2010 OSA

39. R. Leonhardt, B. R. Biedermann, W. Wieser, and R. Huber, "Nonlinear optical frequency conversion of an amplified Fourier Domain Mode Locked (FDML) laser," Opt. Express **17**(19), 16801–16808 (2009).
40. M. K. K. Leung, A. Mariampillai, B. A. Standish, K. K. C. Lee, N. R. Munce, I. A. Vitkin, and V. X. D. Yang, "High-power wavelength-swept laser in Littman telescope-less polygon filter and dual-amplifier configuration for multichannel optical coherence tomography," Opt. Lett. **34**(18), 2814–2816 (2009).
41. M. Y. Jeon, J. Zhang, Q. Wang, and Z. Chen, "High-speed and wide bandwidth Fourier domain mode-locked wavelength swept laser with multiple SOAs," Opt. Express **16**(4), 2547–2554 (2008).
42. K. König, M. Speicher, R. Bückle, J. Reckfort, G. McKenzie, J. Welzel, M. J. Koehler, P. Elsner, and M. Kaatz, "Clinical optical coherence tomography combined with multiphoton tomography of patients with skin diseases," J Biophotonics **2**(6-7), 389–397 (2009).
43. B. D. Goldberg, B. J. Vakoc, W. Y. Oh, M. J. Suter, S. Waxman, M. I. Freilich, B. E. Bouma, and G. J. Tearney, "Performance of reduced bit-depth acquisition for optical frequency domain imaging," Opt. Express **17**(19), 16957–16968 (2009).
44. C. M. Eigenwillig, B. R. Biedermann, G. Palte, and R. Huber, "K-space linear Fourier domain mode locked laser and applications for optical coherence tomography," Opt. Express **16**(12), 8916–8937 (2008).
45. B. R. Biedermann, W. Wieser, C. M. Eigenwillig, G. Palte, D. C. Adler, V. J. Srinivasan, J. G. Fujimoto, and R. Huber, "Real time en face Fourier-domain optical coherence tomography with direct hardware frequency demodulation," Opt. Lett. **33**(21), 2556–2558 (2008).
46. Y. L. Chen, D. M. de Bruin, C. Kerbage, and J. F. de Boer, "Spectrally balanced detection for optical frequency domain imaging," Opt. Express **15**(25), 16390–16399 (2007).

1. Introduction

Optical coherence tomography (OCT) [1] is an imaging modality that can provide three-dimensional (3D) information of the scattering properties of biological samples. However, the slow data acquisition speed of early time domain (TD) OCT systems in the range of ~1kHz usually limited OCT imaging to single B-frame acquisition protocols and usually no full 3D-data sets have been acquired.

The introduction of frequency domain (or Fourier domain; FD) detection techniques with higher sensitivity [2–7] for optical coherence tomography has lead to a dramatic increase in imaging speed. Line rates of ~50-400kHz are now possible [8–14]. At these speeds, it becomes feasible to acquire entire 3D data sets, offering a greatly improved flexibility in image data visualization, analysis, quantification and processing [15–17]. Examples reflecting the advantage of 3D data include (a) the reconstruction of collapsed en face views for absolute registration of OCT scans [18], (b) sectioning and the extraction of arbitrarily curved slices out of the 3D data set [11,12], (c) volumetric quantification of tissue morphology features, e.g. macular holes for diagnosis of disease progression, (d) the reduction of sampling errors caused by missing a sample location in 2D imaging [11], and pseudo optical coherence microscopy for simultaneous high resolution en face projections [19]. Besides these applications, where the high imaging speed is mainly used for acquiring 3D image data, high speed OCT can also give access to the observation of transients, dynamics and rapid changes in samples [20,21], which are simply too fast for slower systems. The third major application of high speed imaging is trading of speed against image quality or functional contrast. Averaging several frames acquired with a high speed system usually yields improved image quality due to reduced speckle content [22]. Also, by advanced image processing algorithms, 3D data acquired at high speed can be used to extract functional image information such as Doppler flow – so speed can also be used to generate functional image contrast [23].

Even though all these applications already demonstrated the tremendous potential of 3D OCT imaging, in most cases the 3D data sets had highly unbalanced numbers of samples in each of the three dimensions, or the acquisition time was too long for routine in vivo imaging of non-trained patients. Typical values for the dimension of 3D data sets are somewhere in the range of 500 x 500 x 100, i.e. 500 pixels per depth scan, 500 depth scans/lines per frame and 100 frames [16,17]. With a 50kHz line rate system, such a data set can be acquired in 1 second. However, roughly isotropic sampling, especially in the two transverse directions, is mandatory for many analysis functions operating on 3D data. Data set sizes of ~500 x 500 x 500 would be desired for most standard projections, ~2000 x 2000 x 500 for high definition *en*

#126756 - $15.00 USD Received 9 Apr 2010; revised 4 Jun 2010; accepted 15 Jun 2010; published 30 Jun 2010
(C) 2010 OSA

face visualizations. Aiming at a maximum acquisition time of ~0.2s for a full 3D scan, OCT line rates between 1MHz and 20MHz are necessary.

This means, for many applications, line rates in excess of 1MHz A-scan rate are highly desired. However, the main problem impeding the increase of imaging rate is the requirement to maintain good image quality. To provide sufficient image quality for most OCT applications, a multi-MHz OCT system should have ~10µm axial resolution in tissue and >95dB sensitivity. There have been two demonstrations of OCT systems with line rates of more than 1MHz:

Choi et al. demonstrated a spectral domain (SD) OCT approach with a 60MHz line sampling rate [24]. However, since their analog detection bandwidth was only 12MHz and only 256 samples per scan before Fourier transformation have been acquired, the effective A-scan rate was 12MHz and hence the maximum resulting voxel rate was 12M·128 = 1.5GVoxels/s. The achieved sensitivity value of 88dB was measured with a 700kHz analog bandwidth for each pixel readout circuit, so only at 700kHz equivalent line rate. A deterioration of the image quality at the highest analog bandwidth of 12MHz was observed.

Moon et al. demonstrated a swept source OCT (SS-OCT/OFDI) approach with a 5MHz line rate [25]. Their analog bandwidth was 4GHz at a sweep duration of 70ns, yielding $2 \cdot 4 \cdot 10^{9} \cdot 70 \cdot 10^{-9} = 560$ samples per sweep. Assuming that the roll-off performance is good enough to achieve usable interference signal frequencies up to Nyquist, the voxel rate is $0.5 \cdot 560 \cdot 5 \cdot 10^{6} = 1.4$GVoxels/s. Due to a sensitivity of 40dB no OCT imaging was demonstrated.

In this paper we demonstrate OCT imaging with good image quality, ~100dB sensitivity and 11µm axial resolution in tissue at more than 4GVoxels/s, more than twice as high as the setups demonstrated previously.

There have been additional reports on non-OCT, high-speed ranging concepts in the MHz range, e.g. by Goda et al. [26], who also used a stretched pulse design. The system was demonstrated in a profilometry application with a spectral coverage of only ~15nm resulting in 227µm axial resolution which is insufficient for biomedical OCT imaging. Only one single trace was acquired, no imaging was demonstrated.

As described, all three previously demonstrated cases suffered from low sensitivity or insufficient axial resolution, preventing OCT imaging with good quality. So up to now, it was unclear, if high quality OCT imaging with multi-megahertz line rates is possible and if typical OCT imaging performance can be achieved at these rates. In this paper we demonstrate OCT imaging with good image quality, ~100dB sensitivity and ~10µm axial resolution in tissue at ~4GVoxels/s, 20MAscans/s, 4 x 3650 = 14,600 frames/s and one volume in 25ms. This speed is sustained over the acquisition time of a full 3D volumetric data set and already accounts for dead time caused by the scanners. To the best of our knowledge, this represents the highest voxel rate as well as the fastest 2D and 3D OCT imaging speed ever reported. Table 1 compares the performance of state-of-the art high speed OCT systems to the results presented in this paper.

To achieve this goal, a series of strategies was applied which are discussed in detail in this paper: (a) A novel, ultra-high speed bulk optic Fabry Perot filter was developed to achieve wavelength sweep rates of up to 5MHz, (b) the unique dual output configuration of buffered [10,13] FDML lasers was used to increase the total output power, (c) a novel multi-spot beam delivery system was developed to reduce aberration, (d) a specially adapted scan protocol was used for reliable volumetric data fusion, (e) a numeric image data phase shift algorithm was applied to enable bidirectional beam scanning on the sample with seamless interlacing and (f) a 4 channel 8-bit analog-to-digital converter (ADC) in combination with four specially designed high-bandwidth dual-balanced photodiodes for reduced excess noise at high electronic bandwidth were used. A thorough analysis of the influence of these different strategies on the total system performance is provided by comparison of three different layouts at speeds between 4 and 20MHz line rate.

#126756 - $15.00 USD Received 9 Apr 2010; revised 4 Jun 2010; accepted 15 Jun 2010; published 30 Jun 2010
(C) 2010 OSA

Table 1. Comparison of Several Recent High-Speed OCT Systems[a]

	P_{20dB} *MPixel/s*	V_{20dB} *MVoxels/s*	*Scan rate MHz*	*Sens. dB*
Setup *B8*	1250	4500 (1100 x 4)	10.4 (2.6 x 4)	104
Setup *B16*	1100	4000 (1000 x 4)	20.8 (5.2 x 4)	98
Setup *F* (with LPF)	450	900 (230 x 4)	4.0 (1.0 x 4)	105
Huber et al. [10]	350	<350	0.37	98
Potsaid et al. [14] 3D mode (conf. C)	100	80	0.25	91
Potsaid et al. [14] (conf. D)	90	<90	0.31	98
Huber et al. [13]	110	<110	0.24	91
Choi et al. [24]	(1500)	(1500)	12.0	<88
Moon et al. [25]	(1400)	(1400)	5.0	40

[a]Values in brackets represent upper limit estimates since neither the 20dB roll-off point nor the 3D scan duty cycle were known. The 88dB sensitivity in [24] was measured at merely 700kHz equivalent scan rate. Voxel rates with "<" sign do not take into account scanner dead times and trigger re-arming. Setup *F* is characterized with the 450MHz low-pass filter. Other groups using the Baser Sprint CMOS camera reach a performance similar to that of Potsaid et al. [14].

1.1. Key parameters for OCT image quality

The 5 most important parameters to characterize an OCT setup are: Sensitivity, roll-off performance (relevant for FD-OCT only), dynamic range, axial resolution, and imaging speed.

Sensitivity specifies the highest possible attenuation in the sample arm (i.e. smallest possible back reflection) which can still be detected. Usually the detection threshold is set where the signal to noise ratio (SNR) reaches 1. Shot noise in the detector, caused by light from the reference arm, fundamentally limits sensitivity. Especially for high imaging speeds, lasers with low relative intensity noise (RIN) are mandatory, because high speed photo-receivers have lower responsivity/trans-impedance gain making higher levels of reference arm power necessary for sufficient total signal gain. In order to avoid excess noise, lasers with good RIN performance, such as FDML lasers [27], are required to reach shot noise limited detection. For good image quality in biomedical applications the sensitivity should be >95dB.

The *roll-off performance* determines the decrease in the OCT signal strength with ranging depth, caused by either the limited instantaneous coherence length of the applied light source in SS-OCT [4,27–29] or the limited overall resolution of the spectrometer in SD-OCT [30]. Although depending on the sample, as a rule of thumb, a good OCT system should provide roll-off values of 20dB or less over 2mm ranging depth, corresponding to R-number values [27] of >0.1mm/dB.

The *dynamic range* is the ratio in signal strength between strongest and weakest reflection which can be measured *simultaneously* within one A-scan. Biomedical OCT images often have a dynamic range of ~35dB, so an OCT system should provide 40-50dB.

Axial resolution in OCT is given by the total spectral width and shape of the light source. For SS-OCT, the spectral width is the wavelength swept range of the light source. In biomedical applications, for good image quality the resolution in tissue should be ≤10µm.

Imaging speed in OCT can be defined as number of depth scans (A-scans) per second, number of frames per second (B-frames) or number of voxels per second. Which one of these values makes more or less sense in a special situation depends on the scanning protocol and the imaging setup; e.g. in optical coherence microscopy (OCM) [31] en face frame rates are used rather than the rate of A-scans per second. In SS-OCT a useful value for the effective voxel rate [32] cannot be simply provided based on the sample rate of the ADC as discussed in the following.

#126756 - $15.00 USD Received 9 Apr 2010; revised 4 Jun 2010; accepted 15 Jun 2010; published 30 Jun 2010
(C) 2010 OSA

1.2. Characterizing OCT imaging speed: Scan rate, pixel rate, voxel rate

In most cases, OCT speed is characterized by the axial depth scan rate (A-scan rate or line rate). For SS-OCT systems, it is given by the sweep repetition rate and for SD-OCT by the line rate of the applied line scan camera. While this figure is undoubtedly important, it alone does not seem very suitable to characterize the imaging speed: For example, most line scan cameras can be operated at higher speed if fewer pixels are used, but this does *not* mean that OCT imaging is getting faster. It merely means that axial resolution and/or imaging range is sacrificed to obtain a higher axial scan rate. The amount of extracted information per time usually stays rather constant. The same argument applies when doubling sweep speed in an SS-OCT system without also increasing the analog detection bandwidth. The extreme cases are systems with en face scanning priority, e.g. in optical coherence microscopy (OCM) [31], where the entire depth scan consists of only one point – in such a case, specifying a line rate would not make sense.

Since the main purpose of OCT imaging is to *extract volumetric information* from a sample and represent it as a 2D/3D data set made up of pixels/voxels, the most meaningful measure for OCT imaging speed is the amount of extracted *information per time*, i.e. 2D pixel rate P and 3D voxel rate V [32]:

$$P = N_P / T_2 V = N_V / T_3.$$

Here, T_2 is the time required to acquire a 2D data set (B-frame) consisting of N_P pixels. T_3 is the time required to acquire a complete 3D data set consisting of N_V voxels and includes reduced duty cycles and dead times, e.g. caused by limited agility of the beam scanning optics, such as flyback and turning times of galvo scanners, trigger re-arming times etc. For a B-frame with N_A depth scans and for a 3D volume composed of N_B B-frames, it is straightforward to define

$$N_P = N_A \cdot Z \, N_V = N_P \cdot N_B = N_A \cdot N_B \cdot Z,$$

with Z as the number of resolution elements per depth-scan. Care has to be taken that the pixels and voxels *can actually carry information*: The roll-off performance of the laser and the applied analog detection setup limit the value of Z. For higher imaging depths in SS-OCT, the response drops due to instantaneous linewidth as well as limitations in the analog bandwidth of the detection path including photodiode, transimpedance amplifier and data acquisition system. This behavior is commonly characterized by the roll-off and its associated R number [27] and puts an upper limit to the value of Z.

The 6dB roll-off figure often used to characterize OCT systems is not suitable for our objective to characterize the number of information-carrying depth samples: Higher speed systems usually have a steeper roll-off expressed in mm/dB and still deliver useful depth information well beyond the 6dB roll-off point [14]. Although good OCT systems have a dynamic range of ~50-60dB [10], OCT images in biomedical application, typically have a dynamic range of merely ~30-40dB [33]. As OCT images are usually viewed on a logarithmic scale, for many biomedical OCT samples, it makes sense to define the −20dB (half of the dynamic range on a log scale) roll-off depth as the highest information-carrying depth when computing the pixel and voxel rates.

For SS-OCT systems *without dead time between sweeps*, i.e. 100% duty cycle, the pixel and voxel rates of a system can be obtained particularly easily by observing the interferometer fringe frequency f at some specific roll-off value. Using the 20dB threshold introduced above, the fringe frequency f_{20dB} at the −20dB roll-off depth is assumed as the highest information-carrying frequency provided that the sampling rate is at least twice as high. The pixel rate P_{20dB} is then equal to this fringe frequency f_{20dB} and the voxel rate V_{20dB} is the pixel rate multiplied with the 3D acquisition duty cycle (fraction of time spent acquiring data). This

#126756 - $15.00 USD Received 9 Apr 2010; revised 4 Jun 2010; accepted 15 Jun 2010; published 30 Jun 2010
(C) 2010 OSA

simple relation holds because f_{20dB} is the highest frequency which actually carries usable image information and hence $Z = f_{20dB}/f_{sweep}$ and $N_A/T_2 = f_{sweep}$. In other words, since f_{20dB} is the highest frequency carrying information, $2 \cdot f_{20dB}$ sampling rate is required for Nyquist sampling and after the FFT, $Z = 2 \cdot f_{20dB}/f_{sweep}/2$ resolution elements remain. Zero padding or faster sampling does increase the number of samples but not the number of information carrying resolution elements Z. However, several techniques using active optical elements in the SS-OCT setup can double this rate [34,35]. Here, we also assume that the axial resolution achieved in the setup is given by the integrated spectrum of the light source and no additional broadening of the axial point spread function occurs.

As an example, a SS-OCT system might run at a bidirectional scan rate of 2 x 50kHz and 100nm spectral width using a 350MHz photo detector attached to a 1GSamples/s (GS/s) ADC. After Fourier transform, each A-scan will consist of 10µs/1ns/2 = 5,000 samples, suggesting Z = 5,000 and a pixel rate of 2·50,000kHz·5,000 = 500MPixels/s. However, one wavelength sweep direction of the bidirectional operation may not be used and the roll-off performance of the source might limit the highest usable fringe frequency to 250MHz, reducing the effective pixel rate to 125MPixels/s. The voxel rate may again be somewhat smaller than this pixel rate due to trigger re-arming delays and delays introduced by the scanning optics. So, not only the sampling rate of the ADC, but also the whole performance of the setup has to be considered.

Similarly, to compute the P_{20dB} pixel rate for spectrometer-based OCT systems, not the *total* number of camera pixels has to be used. Relevant pixels are only those which cover the light source spectrum, *and* the required equivalent number of pixels to resolve the 20dB roll-off depth has to be used when estimating the number of information carrying pixels per second, P_{20dB}. For example, the configuration C in [14] has a 20dB roll-off over 2.0mm which happens to be the computed depth range with 800 pixels on the camera resulting in 400 information carrying pixels in the OCT image. We assume that the spectrum covers all 800 pixels, which means no "hidden zero-padding" by non-illuminated pixels occurs. Then, at 250kHz scan rate, the pixel rate P_{20dB} = 100MHz.

2. Experimental setup

2.1. Design considerations

The main goal of the research presented here was to investigate, up to which speed 2D and 3D SS-OCT imaging is possible with good image quality by simultaneously applying several techniques to increase the acquisition rate. The performance of several different setups is compared.

Two main strategies are applied to scale the OCT imaging speed: Firstly, we use an FDML laser, especially designed for ultra-high speed wavelength sweep operation. Here, an FDML laser is the light source of choice because FDML is a stationary laser operating regime [36,37] and so in most practical cases it provides no fundamental sweep speed limitation [9,29], high output power [38–40], low intensity noise [27], wide sweep range [41], and minor phase noise as well as operation in the 1050nm [13,22], the 1310nm [9,41] and the 1550nm [33,39] range for various types of OCT applications. Second, we use a multi-spot scanning approach with 4 spots on the sample to quadruple the OCT line rate. The concept of our setup is similar to the one described in [40]. It is based on the idea of the multi-beam approach used in the commercial system by Michelson Diagnostics Ltd. (e.g. see [42]), however with transversely separated spots on the sample, reducing thermal stress.

As the depth scan rate increases, the power on the sample has to be increased as well, to maintain high sensitivity. Assuming shot-noise limited detection at 1310nm with a photodiode response of 0.95A/W and a backcoupling efficiency of 75% in the sample arm, a scan rate of 1MHz requires a power of 4.5mW on the sample to achieve 100dB sensitivity. Speed and sensitivity are inversely proportional, so for 20MHz, 90mW would be required which,

#126756 - $15.00 USD Received 9 Apr 2010; revised 4 Jun 2010; accepted 15 Jun 2010; published 30 Jun 2010
(C) 2010 OSA

depending on the scanning protocol, might be above the laser exposure safety limits. However, light-induced stress on the sample can be reduced by using multiple well-separated beams. According to ANSI and European laser exposure standards, on skin the incident power is averaged over a 3mm aperture. If the individual spots are separated by significantly more than 3mm, the sum of the laser power of two or more spots can be higher than the power for an individual spot. A similar approach might relax the power constraints to some extent for retinal imaging, too.

Aiming at very high speed, the major design considerations were:

1. An FDML laser is used as swept laser source with the advantage of good sweep speed scalability at low relative intensity noise.
2. A newly developed high speed sweep filter is driven at the highest possible frequency which still provides sufficient filter response.
3. The concept of buffering [10] is applied to further increase the sweep rate.
4. Two separate booster amplifiers make optimum use of the two outputs from the buffer stage, providing sufficient optical power on the sample.
5. Multiple well-separated spots on the sample increase the effective scan rate and reduce thermal stress on the sample caused by the laser spots.
6. A specially tailored 1GHz photo-receiver system is used for the optimum compromise between analog electronic bandwidth and responsivity / transimpedance gain.

In contrast to spectrometer-based FD-OCT systems, the main cost and complexity of an SS-OCT setup is associated with the laser source itself rather than the detector. The detection using a balanced photo receiver and a fast ADC is easily duplicated [40,42] and allows the use of several distinct imaging spots, scanning different parts of the sample [40]. Buffering [10] quite naturally matches this multi-spot design, since external buffer stages [13] usually have two outputs: Instead of wasting half of the power, each of the two outputs can supply half the number of the spots.

Due to the high fringe frequencies, ADC sampling rates in the GS/s range are required. Especially for economic multi-channel operation, this requirement currently limits the data converter bit depth to 8 bit. However, in agreement with the results reported in [43], we also observe in our system that 8 bits provide enough dynamic range: In Fig. 1 we compare the resulting image quality when data sampled with a 12 bit ADC (400MS/s digitizer by GaGe Applied) is artificially bit-reduced during post-processing. The images were created with a 100kHz SS-OCT system. It is noteworthy that artificial bit reduction to 8 bit during post processing corresponds to an ADC with an effective number of bits (ENOB) of nearly 8 while real world 8 bit ADCs usually have an ENOB of 7.x (e.g. National Semiconductor's 8 bit ADCs ADC08D1000 and ADC08B3000 have an ENOB of 7.4 and 7.1 at 1GS/s and 3GS/s, respectively). Hence, unlike [43], we include images at bit depths below 8 bit in our comparison to show that significant image degradation occurs at an ENOB <7 and real world 8 bit ADCs are suitable for OCT imaging. As a consequence of reduced bit depth, the preamplifier gain of the ADC has to be set more carefully than with 12 or 14bit ADCs so that little dynamic range is wasted.

#126756 - $15.00 USD Received 9 Apr 2010; revised 4 Jun 2010; accepted 15 Jun 2010; published 30 Jun 2010
(C) 2010 OSA

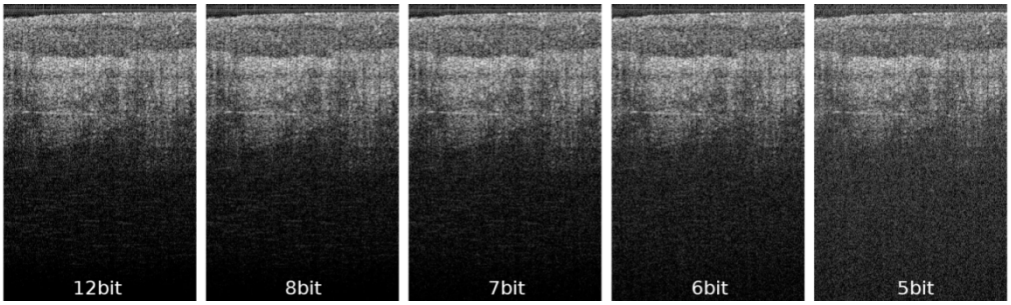


Fig. 1. Comparison of OCT images of the same sample (human finger) acquired with different effective bit depths (ENOB). The actual acquisition was performed with 12 bits and the resolution for individual images was lowered in software during post-processing. Real-world 8 bit ADCs at 1-3GS/s correspond to an image quality similar to the 7 bit image.

Modern digital real-time oscilloscopes commonly provide adequate bandwidth on up to 4 channels with 8 bit each, making the use of 4 imaging spots a natural choice. In our case, the 3D acquisition data size is limited to 64 million samples per spot by the 256Mb storage of the oscilloscope (DPO7104 from Tektronix).

For the spot separation, a value of 2mm is a good overall compromise: Laser safety regulations make use of a 3mm aperture, hence only 2 of the 4 spots account for exposure. The "native" size of a 3D data set is then 8mm along the spot separation axis supporting 330 independent scan steps for a spot size of 24µm on the sample. Using 2-4 sampling points per mode field diameter suggests roughly 600-1200 scans per frame. Alternatively, a smaller spot separation could be used in order to trade in increased light-induced stress for higher scan range flexibility. For example, with 0.5mm spacing along the slow scan axis, the "native" 3D cubes can have any even length (2, 4, 6, 8mm,…) along the slow axis. However, this also comes with increased post-processing effort as for 8mm, 16 individual 3D-sub-cubes would have to be merged.

2.2. Balancing sweep frequency and buffering multiplier

In FDML, the sweep frequency of the laser is limited by the wavelength tuning speed of the optical band pass filter, which, in our implementation is a piezo electric actuator (PZT) driven Fabry-Pérot filter. As the wavelength tuning speed of a sinusoidally driven filter is a product of amplitude and frequency, either of these parameters can be increased to achieve higher tuning speeds. Especially when increasing the drive amplitude of the filter, the sweep of interest fills only a fraction of the period and therefore the concept of buffering can be used to fill up the duty cycle to 100% with delayed copies of one sweep [10,13]. Depending on the type of PZT used in the Fabry-Pérot filter, there are usually several mechanical resonances where the filter can be driven over an optical bandwidth of typically 100nm which gives adequate resolution in OCT. We found that the roll off performance of the FDML laser is improved if the filter is driven at a higher resonance frequency and lower amplitude, probably because the shorter FDML cavity length introduces less dispersion and self phase modulation [27,37]. In contrast, the buffering factor, i.e. the number of sweep copies, seems to have no observable effect on OCT performance, at least up to 16x buffering. Buffer factors above 16x are normally unpractical since they demand very large filter tuning ranges.

To find the maximum sweep speed of the filter, the optical response of each resonance frequency of the filter has been checked, and the one which allowed for fastest wavelength tuning speed chosen. Next, the highest possible sweep range was determined experimentally and an adequate buffer stage (4x, 8x or 16x) was built.

#126756 - $15.00 USD Received 9 Apr 2010; revised 4 Jun 2010; accepted 15 Jun 2010; published 30 Jun 2010
(C) 2010 OSA

2.3. FDML laser sources

Three different FDML laser sources, called *F*, *B8* and *B16*, were built and compared. The first source, *F* (see Fig. 2), features a *fiber*-based Fabry-Perot filter (FFP-TF, LambdaQuest LLC - special "no-gel" version with reduced damping), driven at 257kHz, followed by a 4x buffer stage resulting in a sweep rate of 1.0MHz. The sweep rate was limited by the response and the thermal stress of the piezo crystal in the filter. The other two lasers, *B8* and *B16* (see Fig. 3), use a home-built *semi-bulk optics* Fabry-Perot filter (BFP-TF) driven at 325kHz, followed by an *8*x and *16*x buffer stage, respectively. The *B8* laser has a sweep range of more than 100nm at 2.6MHz scan rate while *B16* provides a scan rate of 5.2MHz but is limited to 80nm by the filter: Larger tuning ranges were prevented by mechanical contact of the filter facets. The BFP-TF simply consists of two 0.5" mirror mounts holding the fibers, and the cavity makes use of a glass plate with reflective coating. For a compilation of the various parameters, see Table 2, which also includes the scanning protocol and 2D/3D-data set sizes in imaging application.

Table 2. Key Parameters of the 3 Different Setups[a]

	F	***B8***	***B16***
FDML resonance frequency	257 kHz	325 kHz	325 kHz
Buffer factor	4	8	16
Eff. sweep rate per spot	1.0 MHz	2.6 MHz	5.2 MHz
Sweep range	110 nm	100 nm	80 nm (filter limited)
Filter FSR and width (–3dB)	205 nm, 340 pm	330 nm, 380 pm	330 nm, 380 pm
Linewidth (FWHM)	80 pm	150 pm	240 pm
Laser output power	4 x 6.35 mW	8 x 2.3 mW	16 x 1.17 mW
Booster output pwr (no mod.)	2 x 90 mW	2 x 100 mW	2 x 85 mW
Power on sample	4 x 16 mW (WS)	4 x 30 mW	4 x 25 mW
Measured sensitivity (SNR = 1)	105 dB	104 dB	98 dB
Shot noise limit	105 dB	104 dB	100 dB
Analog bandwidth	450 MHz (LPF)	1 GHz	1 GHz
Acquisition sample rate	1.25 GS/s	2.5 GS/s	2.5 GS/s
R number (roll-off)	0.34 mm/dB	0.21 mm/dB	0.10 mm/dB
–20dB roll-off OCT depth	6 mm	4.8 mm	2.3 mm
RIN@1GHz (sweep average)	1.0%	0.7%	1.5%
Samples per depth scan	1200	950	475
Depth resolution in tissue	11 um (WS)	11 um	13 um
3D scan size (D x L x F x S)	1200 x 600 x 85 x 4	950 x 640 x 100 x 4	475 x 1280 x 100 x 4
3D scan duty cycle	50%	90% (bidir)	90% (bidir)
Max fringe frequency (20dB)	(760 MHz)	1.25 GHz	1.1 GHz
2D depth scan line rate	**4.1 MHz**	**10.4 MHz**	**20.8 MHz**
Sustained 3D depth scan rate	2.1 MHz	9.4 MHz	18.7 MHz
Sust. 2D pixel rate (1 spot)	450 MHz	1.25 GHz	1.1 GHz
Sust. frame rate (4 spots)	**3.3 kHz**	**14.6 kHz**	**14.6 kHz**
Sust. 3D voxel rate (4 spots)	**900 MVoxels/s**	**4.5 GVoxels/s**	**4.0 GVoxels/s**

[a]Laser *F* applied booster current modulation to Welch shape (WS), so that no software apodizing was necessary. Lasers *B8* and *B16* used constant booster current and a Hann shaped window function for imaging; their measured resolution is specified without apodizing. "bidir" denotes bidirectional scanning. The 3D scan size is limited by oscilloscope storage (256Mb): D x L x F x S specifies number of depth samples x number of depth scan lines per frame x number of frames x number of spots. For imaging at 1.25GS/s, a separate low pass filter (LPF) was used, so although the 20dB roll-off frequency is 760MHz without the LPF, the detection bandwidth of 450MHz has to be used for pixel and voxel rate computations.

#126756 - $15.00 USD Received 9 Apr 2010; revised 4 Jun 2010; accepted 15 Jun 2010; published 30 Jun 2010
(C) 2010 OSA

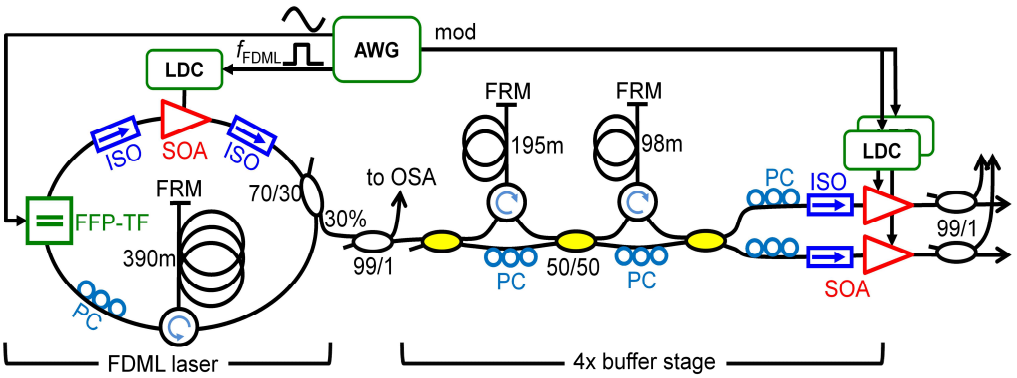


Fig. 2. FDML laser "*F*" with fiber-based filter (FFP-TF), followed by a 4x buffer stage with 2 booster SOAs. (FRM: Faraday rotation mirror; ISO: isolator; AWG: arbitrary waveform generator; PC: polarization controller; LDC: laser diode controller)

The basic setup of the FDML laser *F* is similar to the ones described previously [9,13,44,45]. To minimize polarization effects, laser *F* makes use of circulators in the cavity as well as in the buffer stage. We found that due to the highly polarization dependent gain of the booster semiconductor optical amplifiers (SOA, Covega type BOA-1132), reliable operation of all buffered sweeps over at least 100nm required the use of circulators and polarization controllers (PC) in each branch. In contrast to this, the faster lasers *B8* and *B16* and their buffer stages could be operated very well without circulators, probably because the shorter fiber spools reduced polarization effects.

Both setups include a 99/1 coupler between the laser and the buffer stages for wavelength monitoring on an optical spectrum analyzer (OSA). Further 99/1 couplers after each buffer SOA were integrated for sweep amplitude shaping [45] and monitoring of polarization controller adjustments.

The output coupler in the FDML laser cavity was placed after the SOA and not after the filter so that more power is available for the buffer stages and the booster SOAs. Although this design features two successive SOAs without filter in between, we found that it outperforms approaches where the output coupler is placed after the filter: The booster SOA *does* amplify ASE from the laser SOA, but the substantially higher input power saturates the booster and results in good suppression of booster ASE background. The overall ASE background therefore compares favorably to setups where the ASE-free *post-filter* laser output is boosted.

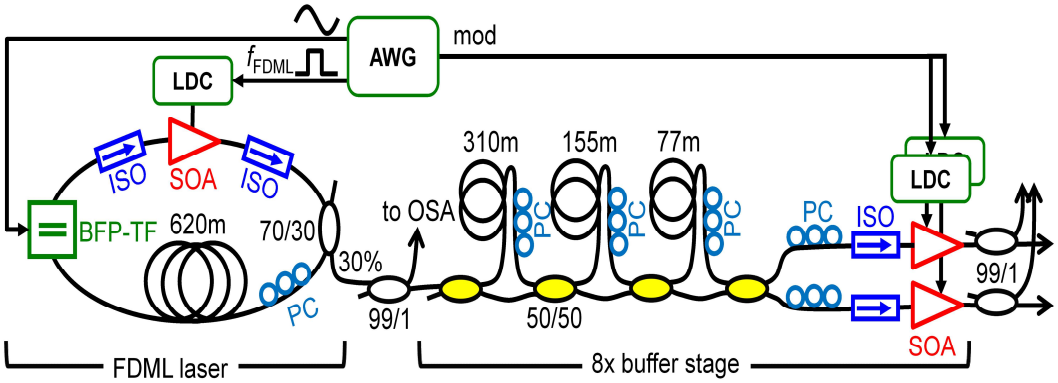


Fig. 3. FDML laser "*B8*" with bulk Fabry-Perot tunable filter (BFP-TF), followed by an 8x buffer stage with 2 booster SOAs. The laser "*B16*" differs merely by adding another buffer stage element with 39m fiber delay.

#126756 - $15.00 USD Received 9 Apr 2010; revised 4 Jun 2010; accepted 15 Jun 2010; published 30 Jun 2010
(C) 2010 OSA

All filters were driven by a multichannel arbitrary waveform generator (AWG; TTi TGA12104) followed by a home-built high speed piezo driver. Special, home built high-speed laser diode controllers (LDC) modulated the SOA current to enable FDML lasing over a fraction of a filter cycle only, as required for buffering (Laser *F*: duty cycle 25%, driver WL-LDC10D from Wieserlabs (www.wieserlabs.com), 6MHz bandwidth; lasers *B8* and *B16*: duty cycles 12.5% and 6.25%).

2.3 Multi-spot interferometer

The OCT sample is scanned with 4 separate laser spots to effectively quadruple the 3D acquisition speed. Figure 4 shows the 4-spot interferometer. Each of the two boosted outputs from the buffer stage supplies two spots. A fused fiber coupler splits the light from the buffer SOA into reference (20%) and sample arm (80%). The reference arm includes an adjustable common freespace delay of ~30cm matched to the free air path length of the sample arm for equal dispersion. Each of the spots has an individual adjustable delay (~2cm) to match the coherence gate among the spots. By slightly misaligning its freespace coupling, the reference arm power can be attenuated. The circulator in the reference arm serves two purposes: It compensates the dispersion introduced by the circulator in the sample arm and effectively reduces the mechanical length of the freespace common delay by a factor of 2. This interferometer design has the advantage that less power is wasted than by using a 50/50 coupler and an attenuator in the reference arm.

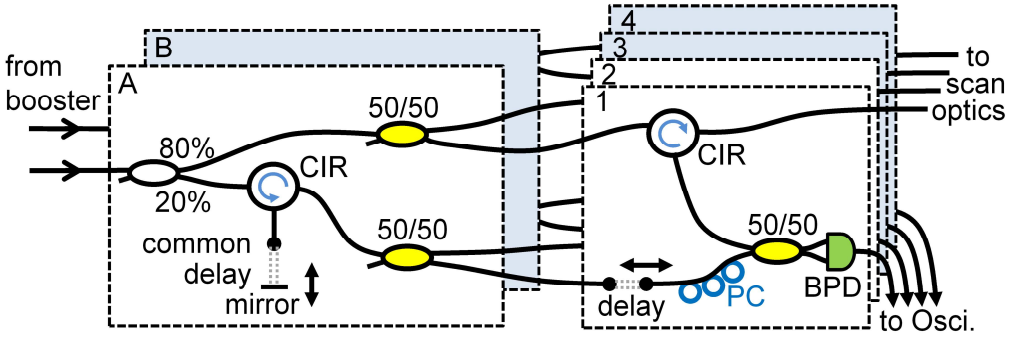


Fig. 4. 4-spot interferometer (CIR: circulator; BPD: balanced photo diode).

The fringe signal contrast is maximized for each spot using a polarization controller (PC). The signal is detected with a home built low-noise dual balanced InGaAs photoreceiver (BPD) with 1GHz bandwidth and 3300V/W trans-impedance gain (WL-BPD1GA from Wieserlabs (www.wieserlabs.com)). The photoreceiver is AC-coupled with a lower cutoff frequency slightly higher than the sweep repetition rate, in order to suppress background signal introduced by the chromatic imbalance of the 50/50 coupler in front of the detector. Fringe signals from an isolated reflection for setup *B16* are shown in Fig. 6 (right). Especially for large reference arm power near the excess noise limit, this chromatic imbalance forms the major electrical signal contribution on the ADC and hence limits the achievable dynamic range. By setting the lower 3dB cutoff frequency to $2 \cdot f_{sweep}$, signal contributions at the sweep repetition frequency are suppressed by 9dB. Hence, the first 2 depth resolution elements (which are normally unusable anyway) are traded in for typically 3-6dB more dynamic range.

2.4. Multi-spot scanner optics

Light from the 4 individual sample arms from the interferometer is focused on the sample at 4 different locations separated by 2mm along the slow axis of the galvanometer (galvo) mirrors of the beam scanner unit. Apart from aberrations in the objective, the axial focus plane is the same for all spots. This setup (see Fig. 5, left) allows the imaging system to simultaneously acquire 4 complete 2D B-frames along the fast galvo axis, with a spacing of 2mm.

#126756 - $15.00 USD Received 9 Apr 2010; revised 4 Jun 2010; accepted 15 Jun 2010; published 30 Jun 2010
(C) 2010 OSA

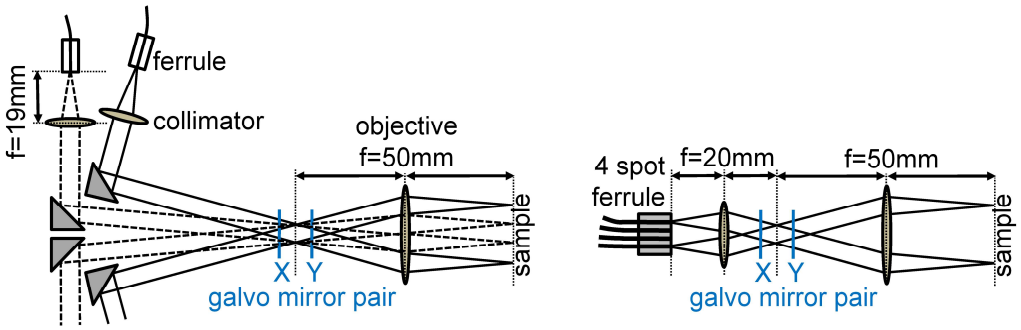


Fig. 5. Left: 4-spot imaging setup with XY-galvo scanner and objective. Right: Alternative approach with multi fiber ferrule.

For 3D imaging, the fixed 2mm distance requires that the 4 3D volumes of each spot cover an 8mm range along the slow axis. In practice, to help merging the data sets, we chose to scan slightly more than 2mm along the slow axis to obtain at least ~10% overlap between the 3D volumes acquired by the individual spots.

Each individual sample arm fiber is first collimated with a 19mm achromatic doublet. Prismatic mirrors for beam steering ensure all 4 beams cross each other right between the two galvo mirrors. This way, the required free aperture of the mirrors is just insignificantly larger than for a single collimated beam. A 50mm achromatic doublet forms the objective. It is placed 50mm from the galvo mirrors to achieve telecentric scanning.

The sample is located in the focus 50mm in front of the objective. The 50:19 lens ratio results in a theoretical spot size (mode field diameter) of 24µm on the sample. 2mm spot spacing is achieved by an angle of 2.3° between individual beams. This requires a distance >14cm between the galvo mirrors and the prismatic mirrors due to the collimated beam diameter of 5.5mm.

Since the achromatic doublet is not specially corrected for off-axis projection, the backcoupling efficiency for the outer beams (~40%) is reduced compared to the central beams (~60%). Furthermore, the axial focal position differs slightly which can be compensated by adjusting the individual collimators. Despite these differences, Fig. 6 (left) shows that OCT imaging performance of all 4 spots is similar.

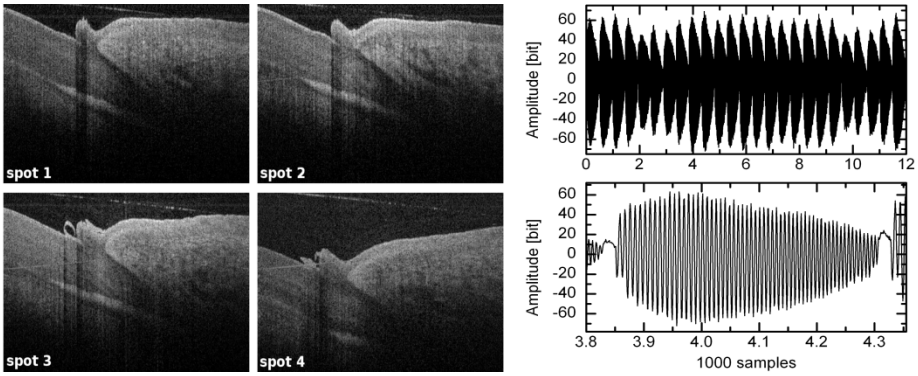


Fig. 6. Left: Frames from the 3D data set shown in Fig. 12 (center) acquired with setup *B8* at 2.6MHz depth scan rate. Each frame is from a different spot of the multi-spot setup and shows that all 4 spots deliver similar OCT performance. Each frame consists of 600 A-scans with 512 depth samples each; the 2D frame rate during 3D scanning was ~3.6kHz. Right: Interference fringes from the setup *B16* acquired at 2.5GS/s as used for imaging. The upper graph shows 25 sweeps and the lower graph is a magnification of the same data set showing a single sweep.

#126756 - $15.00 USD Received 9 Apr 2010; revised 4 Jun 2010; accepted 15 Jun 2010; published 30 Jun 2010
(C) 2010 OSA

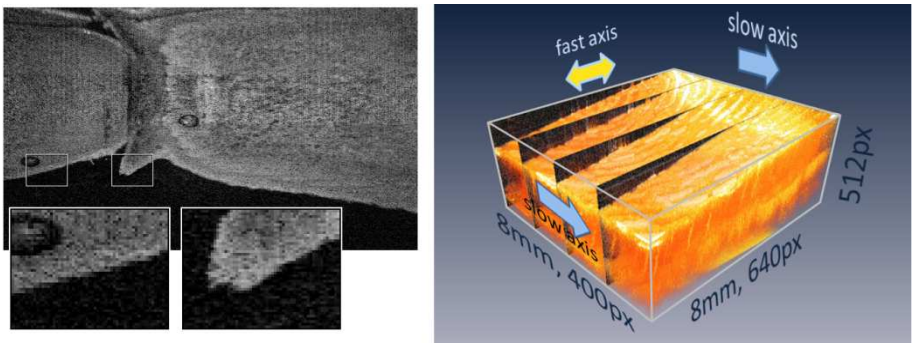


Fig. 7. Left: En-face cut (605 x 360 pixel) at depth position 100 samples (0.7mm) showing human nailfold. The fast axis is oriented horizontally. Small images show magnifications of selected image parts. Zipper artifact caused by bidirectional scanning and multispot operation are hardly visible. Right: Typical nearly-isotropic scanning protocol for 3D OCT imaging at 4 x 2.6MHz with setup *B8*. The final 3D data set has 512 depth samples, 605 A-scans per B-frame and 360 B-frames. Setup *B16* is similar but makes use of twice as many A-scans on the fast axis while providing half the number of depth samples. The shown 3D data was acquired with setup *B16* at 4 x 5.2MHz line rate (14.6kHz frame rate) and shows human skin with well visible perspiratory glands.

We also investigated an alternative realization of the multi-spot imaging setup, using a home built multi fiber ferrule (Fig. 5, right). This approach was similar to the one used in [40]. For a spot spacing of 2mm on the sample, the ferrule requires a fiber spacing of 0.8mm and forces a clear aperture >8mm on a 20mm collimator. Using an achromatic doublet as collimator, we found that the outer spots suffer from poor backcoupling efficiencies of merely ~10% (inner spots: ~45%) due to aberrations caused by these off-axis beams. Hence, without a specially designed multi-element objective, for our setup, the multi-fiber ferrule approach is inferior compared to the setup described earlier. Hence, all the data presented in the following was acquired with the multi-collimator setup.

2.5. 3D data acquisition

The main goal of 3D imaging is to generate an isotropically sampled 3D cube with roughly equal numbers of voxels in both scanning directions and a roll-off limited number of voxels along the depth direction. From the roll-off characteristic of the setup *B8*, a sample rate of 2.5GS/s is the best available choice (1.25GS/s is below Nyquist while 5GS/s would waste storage). A typical A-scan acquired this way consists of 950 samples resulting in 475 depth samples after Fourier transform (alternatively 512 samples with 8% zero padding). The available oscilloscope storage then allows for a raster grid of 640 A-scans per B-frame and 400 B-frames. Accounting for 15% overlap between the spots, the resulting 3D data set is 640 x 340 x 512 voxels. For this protocol, a B-frame is acquired in only 246µs equivalent to a frame rate of 4065Hz for each spot. Similar considerations led to the 3D scan size of setup *F* with 340 frames in total and 600 scans per frame (see Table 2).

2.6. Bidirectional scanning and removal of "zipper" artifacts

Imaging at high speed puts high stress on the fast axis galvo scanner and pushes non-resonant scanners to their mechanical limits. In the slow 4MHz setup *F,* the galvo scanner was driven with a modified triangle waveform resulting in a linear scan during 50% of the time and deceleration, flyback and acceleration in the other 50%. This 50% scan duty cycle effectively decreases the sustained 3D voxel rate since half the time is spent waiting for the mirror to return. For setups *B8* and *B16*, this gets even worse: It turned out that 246µs/B-frame from setup *B8* is already at the limit of what the galvo mirror can do in *sinusoidal* motion. For this reason, the data sets from *B16* feature a scanner-limited number of 1280 A-scans per B-frame.

#126756 - $15.00 USD Received 9 Apr 2010; revised 4 Jun 2010; accepted 15 Jun 2010; published 30 Jun 2010
(C) 2010 OSA

To work around the scan speed limitation imposed by dead times during galvo mirror flyback and in order to compensate for the sinusoidal motion of the mirrors at the required high speeds, we use a bidirectional scanning protocol for the fast axis. Bidirectional scanning with non-resonant galvo scanners usually generates "zipper"-like artifacts caused by off-axis vibrations of the mirror. Scans in forward and backward direction exhibit slightly different appearance showing up as an interlaced line artifact. To remove this artifact, prior to imaging, we performed a 3D scan of a film stripe target with 0.5mm line spacing with the same bidirectional scan parameters as used later for imaging the sample of interest. The lines were oriented parallel to the slow axis. The resulting 3D data set was integrated along the depth direction to obtain a flattened 2D "top view" on the stripe target. This image gives good contrast and allows to identify 16 individual stripes for an 8mm scan range. The B-frame sampling trigger was adjusted so that forward and backward scans show up symmetrically and hence cover the same image area. All odd and all even frames were averaged to obtain two stripe cuts, corresponding to forward and backward scan directions. In these cuts, the stripes show up as peaks with good contrast. They are not equally spaced because of the sinusoidal motion of the scanner. Due to bidirectional scanning, odd and even frames differ in their scan direction, so the first peak in the forward cut can be identified with the last peak in the backward cut. By identifying each of the 16 peaks in both scan directions, a 5th order interpolation polynomial can be obtained for each scan direction. These 2 polynomials stay valid as long as the scan parameters remain unchanged and were used to convert all B-frames during subsequent 3D imaging. The described method is highly effective and the "zipper"-like stripe effect caused by errors introduced during the process is barely visible in volumetric data renderings as well as in en-face cuts (see Fig. 7).

2.7. Merging data sets from multiple spots

For 3D image generation, 4 individual 3D cubes, one for each spot, have to be fused into one. The scan ranges were chosen to overlap by about 15%, so that 4 x 100 B-frames could be merged into one 3D data set containing 340 frames. The overlapping frames were simply cut out from one of the data sets but help aligning the 4 individual cubes. Although the optical setup was adjusted carefully, we found that a shift of 1-2 voxels along the fast axis was necessary for smooth transition. Furthermore, due to slightly different reference arm power and backcoupling efficiencies, the cut levels during post-processing were set differently for each sub-cube to achieve equal contrast and brightness. Once adjusted, offsets and cut levels were found constant throughout the imaging session.

The scan optics (Fig. 5) uses pre-objective telecentric scanning so that the optical path length stays constant during scanning and hardly any depth curvature is introduced in the OCT data. This is especially important when merging data sets from multiple distinct imaging spots to avoid introducing image artifacts. The almost completely seamless image fusion of the 4 different 3D data sets as well as the artifact removal during line interlacing by our algorithm is shown in Fig. 7 (left).

3. Results

3.1. Characterization of the swept laser sources

All presented setups were characterized for several properties including power, sweep range, RIN, sensitivity and measured resolution. The numbers are summarized in Table 2.

All lasers exhibit good relative intensity noise (RIN) performance. Inter-sweep RIN values [27] covering a detection bandwidth from 5MHz to 1GHz were <1.5% (see Table 2). This is especially important for high speed imaging because usually, lower trans-impedance gain in high speed photodiodes has to be compensated by increased reference arm power.

#126756 - $15.00 USD Received 9 Apr 2010; revised 4 Jun 2010; accepted 15 Jun 2010; published 30 Jun 2010
(C) 2010 OSA

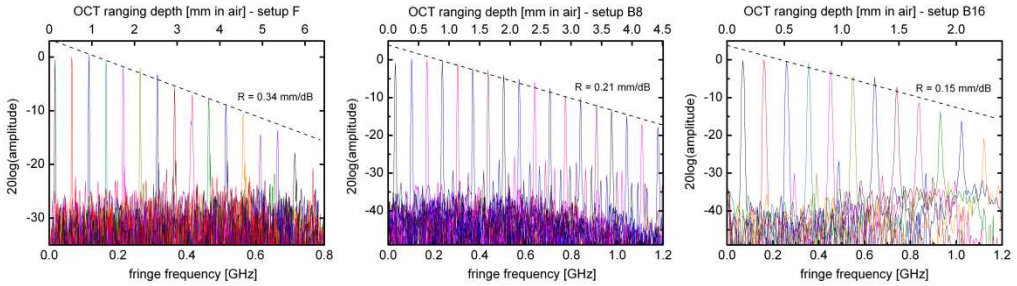


Fig. 8. Roll-off characteristics of the lasers (*F, B8, B16*), measured after the booster SOA. The lasers with bulk filters show significant side lobes caused by amplitude modulation over the sweep introduced by an uncoated glass surface within the home built Fabry Perot filter.

Lower-noise laser sources allow for higher reference arm power levels before excess noise from the laser starts to dominate the total observed noise. We found that especially for the setups *B8* and *B16*, the fine adjustment of the FDML sweep frequency to values with low RIN was necessary to achieve good sensitivity and OCT images free of excess noise.

Setups *F* and *B8* reach shot-noise limited detection when a suitable reference arm power is adjusted; setup *B16* comes very close lacking only 2dB to shot noise limit. We used a reference arm power of ~1mW for all three configurations; the oscilloscope's vertical gain was set to achieve a full range between 100 and 400mV for sensitivity measurements and imaging. Due to this high reference arm power, chromatic imbalance in the interferometer creates a large background, despite the use of a dual balanced detection. This chromatically imbalanced background has previously been identified to prevent shot noise limited detection in certain setups [46].

Here, we find that for configurations *F* and *B8*, the excellent RIN performance of the FDML lasers [27] allows to reach shot noise limited detection. For configuration *B16*, its increased RIN makes the sensitivity fall 2dB short of shot noise.

The measured sensitivity (as specified in Table 2) was obtained by use of a calibrated reflector in the sample arm (filter with OD 2.8 in front of a mirror) and observing the resulting SNR of the OCT signal (i.e. peak height to RMS noise). It represents the true sensitivity of the imaging setup despite its back-coupling losses. The corresponding shot noise limited sensitivity in Table 2 was computed from the sample arm power for an SNR of 1 and reduced by the sample-to-detector back-coupling ratio. This means, a lossless beam delivery unit would increase both values in the table.

The roll-off performance of the sources is shown in Fig. 8. It is noteworthy that for setups *B8* and *B16*, the 20dB roll-off depth occurs at fringe frequencies above 1GHz which is above the analog bandwidth of our oscilloscope. These setups also exhibit distinct sharp side lobes at ~100MHz (setup *B8*) and ~200MHz (setup *B16*) offset caused by laser amplitude ripples introduced by the home-made bulk optics Fabry-Perot filter.

3.2. Imaging performance

For setup *F*, due to mentioned constraints in acquisition memory, the sampling rate was set to 1.25GS/s and hence a 450MHz lowpass filter was inserted to avoid aliasing of signals above Nyquist frequency. Setups *B8* and *B16* were acquired at 2.5GS/s with a bandwidth of ~1GHz; see Table 2 for a summary. We find that the images, especially those generated with the setup *B8* at a sweep rate of 2.6MHz, show remarkable quality similar to images acquired at much lower speed.

#126756 - $15.00 USD Received 9 Apr 2010; revised 4 Jun 2010; accepted 15 Jun 2010; published 30 Jun 2010
(C) 2010 OSA

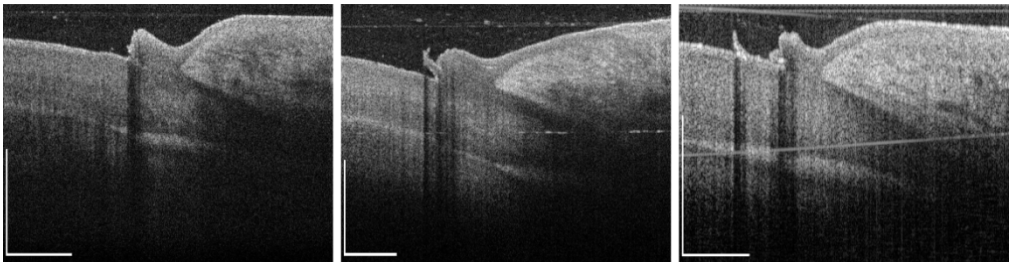


Fig. 9. Direct comparison of imaging performance of the three setups *F*, *B8* and *B16* (left to right): The images show in-vivo B-frames of human finger (nail bed) acquired at 1.0, 2.6 and 5.2MHz depth scan rate, respectively. All three images are single non-averaged B-frames consisting of 1250 A-scans each. The corresponding acquisition times were 1.3ms, 480µs and 240µs, respectively. Scale bars denote 1mm in water.

Figure 9 is a direct comparison of OCT imaging performance of the three presented setups. The images showing in-vivo nail bead of the same finger consist of 1250 A-scans each, and were not subject to averaging. The acquisition times were 1.3ms, 480µs and 240µs, respectively (only 1 of the 4 imaging spots used). We find the quality of all three images is remarkably good, although the image of setup *B16* exhibits larger speckle size due to the reduced sweep range.

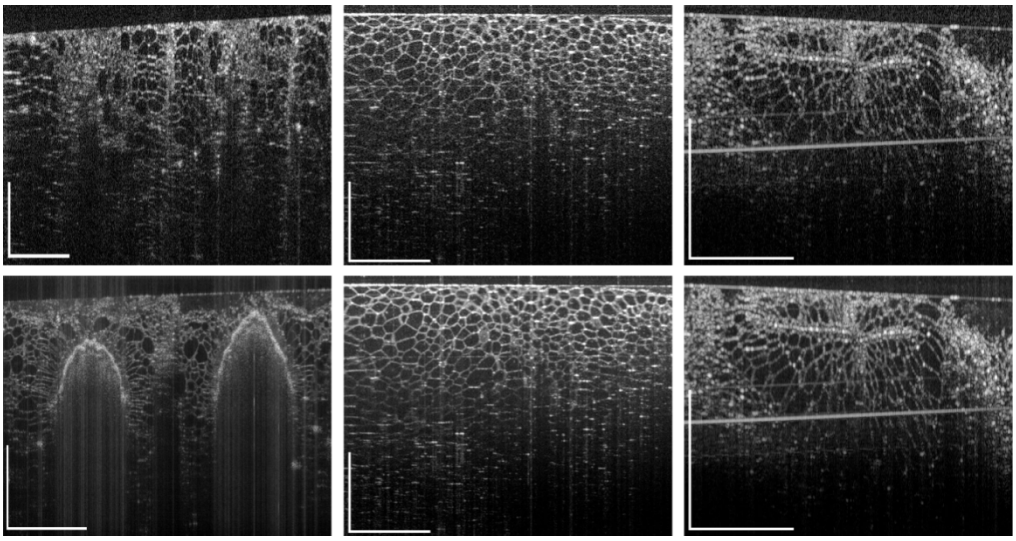


Fig. 10. Image comparison of the setups *F*, *B8* and *B16* (left to right) at 1.0, 2.6 and 5.2MHz depth scan rate showing cellular structures of kiwi (left) and cucumber (center and right). The top row shows single B-frames, each consisting of 800 A-scans and acquired in 800µs, 310µs and 155µs, respectively. The bottom row shows gliding frame averages over several B-frames: For setups *B8* and *B16* (center, right), the lower images are gliding averages over 5 such B-frames as shown on the top row and taken in intervals of ~1s. For setup *F* (left), 10 frames consisting of 1024 A-scans of a different location in the kiwi were averaged in acquisition intervals of ~1s. Scale bars denote 1mm in water.

#126756 - $15.00 USD Received 9 Apr 2010; revised 4 Jun 2010; accepted 15 Jun 2010; published 30 Jun 2010
(C) 2010 OSA

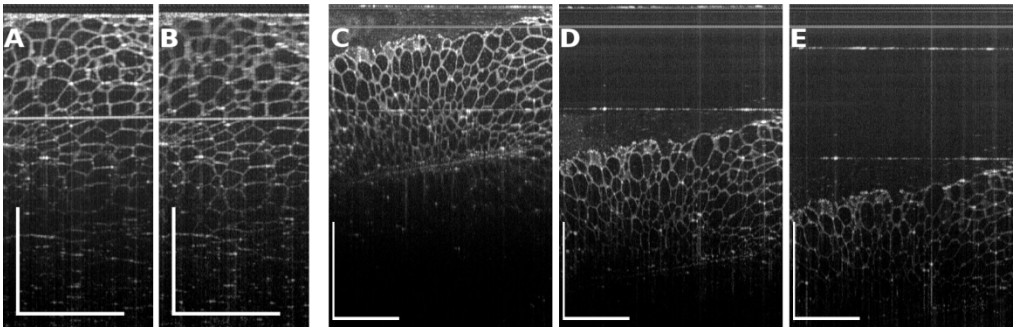


Fig. 11. Images of cucumber taken with setup *B8* at 2.6MHz depth scan rate. A, B: Increased penetration by focusing deeper into the sample while sacrificing sharpness near the surface. (208 A-scans cut out, slow gliding average over 5 frames) C-E: Imaging the same sample at 3 different positions shows that the 2.6MHz system can deliver signal even from 3mm imaging depth as expected from the roll-off performance (670 A-scans cut out, slow gliding average over 5 frames). Scale bars denote 1mm in water.

A similar comparison can be seen in Fig. 10 showing cellular structures (kiwi slice for setup *F* and cucumber slices for setups *B8* and *B16*). The top row shows single B-frames made up of merely 800 A-scans (acquisition time: 800µs, 310µs, 155µs). On the bottom row, gliding averages over several B-frames taken in intervals of ~1s are shown. The gliding average uses an exponential damping of the image content of previous frames by computing each pixel as $p_{t+1} = [p_{t-1} \cdot (n-1) + p_t]/n$ where n is the specified number of averaged frames. The interval time is given by the live preview frame rate of our software and dominated by data transmission time over network and additional delays found to be necessary during remote configuration of the oscilloscope.

Figure 11 (right) shows the behavior of the imaging system regarding OCT ranging depth. It can be seen that even at 2.6MHz depth scan rate, the OCT depth range is larger than the depth of field of the applied 50mm objective and covers all the ranging depth expected from the roll-off performance (Fig. 8). In the images a couple of horizontal line-artifacts can be seen: The well-pronounced line just above the figure caption letters is of constant brightness across all A-scans. The exact origin of this line is unknown, however, it can be suppressed by background subtraction. Therefore, it is barely visible in most images, but in the image series C, D, E, an outdated background data set had been used. Slight drift in the laser requires to capture a background data set (consisting of the average of 100 A-scans) every ~5 minutes.

The lower line in C is the mirrored reflection from the glass surface of the 1mm glass plate which holds the cucumber sample. In the image C, this line is the folded back mirror image of the *near* glass surface and hence strikes right through the cucumber sample. In D, this line is the *far* glass surface which has direct contact to the cucumber sample. It appears to be at the same depth just as a matter coincidence but in fact these 2 lines in C and D are different glass surfaces. In E, both the glass surfaces can be seen. The *near* glass surface is not visible in D because it was positioned right at zero delay and cropped away together with the first 5 depth samples of each image. As can be seen in Fig. 11, A and B, the penetration depth can be increased by focusing deeper into the sample when sacrificing sharpness near the surface.

Complete 3D reconstructions of volumetric data sets can be seen in Fig. 12; a corresponding 3D movie for each setup is available online.

#126756 - $15.00 USD Received 9 Apr 2010; revised 4 Jun 2010; accepted 15 Jun 2010; published 30 Jun 2010
(C) 2010 OSA

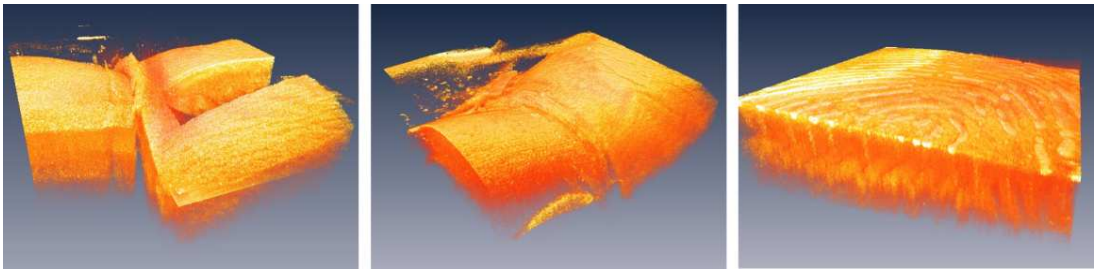


Fig. 12. 3D reconstructions of OCT data: 3D movies online. Left: (Media 1) Human finger near the nail with certain parts cut out to reveal internal structure. Data acquired with setup *F* at 1MHz scan rate. The data set consists of 306 frames, each frame has 600 A-scans with 350 depth pixels after cropping. Center: (Media 2; high-resolution version: Media 3) Human finger near the nail consisting of 340 frames, each frame made up of 600 A-scans containing 512 depth samples (cropped to 350 pixels in depth). Imaging was performed with setup *B8* at 4 x 2.6MHz depth scan rate. The complete acquisition (including galvo dead times) was performed in 25ms. Right: (Media 4) Human skin taken with setup *B16* at 4 x 5.2MHz depth scan rate. The 3D cube consists of 360 frames with a size of 1200 A-scans. Depth samples were zero-padded to 512 samples after FFT and then cropped to 330 pixels. The total acquisition time including galvo dead time was 25ms.

3.3. Volume averaging as new method for speckle reduction in multi-MHz OCT

Image quality in multi-kHz systems can be improved by averaging multiple B-frames. Not only shot noise and noise from the acquisition system is reduced but usually also the speckle "noise" is lowered due to sample motion, thermal motion diffusion and similar effects, resulting in a better image. However, in very fast OCT systems, such as the ones presented here, B-frame averaging at full acquisition speed does not significantly reduce speckle content: As can be seen in Fig. 13, the speckle pattern is found to be fairly stable over successive B-frames acquired at a rate of ~2kHz. While the background noise is reduced, the speckle pattern stays nearly unaffected.

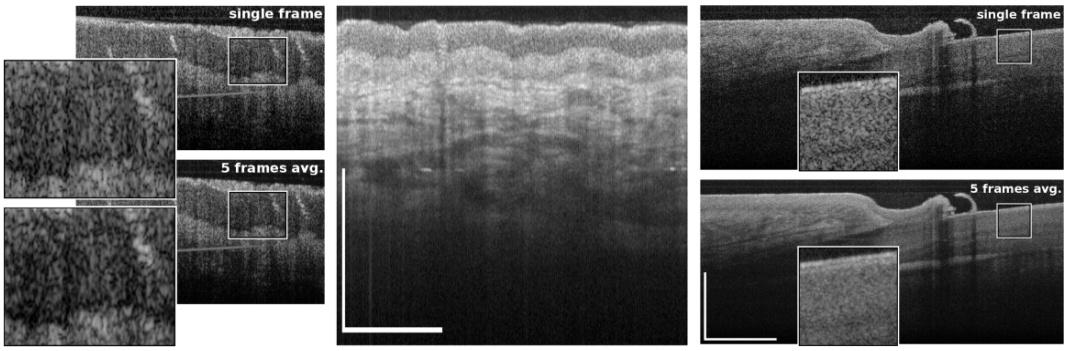


Fig. 13. Comparison of different averaging protocols. Left: Single B-frame (top) with 600 A-scans and an average over 5 such B-frames (bottom). The images were acquired with setup *B16* at 5.2MHz line rate and show human skin with visible perspiratory glands. The averaged frames were acquired at a rate of ~2kHz and show stable speckle behavior as can be seen in the magnified parts. Center: In-vivo image of human skin (finger midjoint) taken with setup *B8* at 2.6MHz depth scan rate. The shown image is a gliding average over 5 consecutive B-frames each consisting of 700 depth scans and acquired at a frame rate reduced to ~1Hz. The image not only shows remarkable penetration depth but also reduced noise and speckle. Right: Images of human nailfold with 1200 A-scans taken with setup *F* at 1MHz depth scan rate. The top image is a single B-frame while the bottom image is an average of 5 such B-frames spaced apart by 12µm/frame along the slow axis and acquired at a frame rate of ~300Hz. The magnifications show the speckle reduction effect. Scale bars denote 1mm in water.

#126756 - $15.00 USD Received 9 Apr 2010; revised 4 Jun 2010; accepted 15 Jun 2010; published 30 Jun 2010
(C) 2010 OSA

If, in contrast, B-frame averaging is performed at a slower frame rate, the speckle contrast reduces, as can be seen in Figs. 10 (bottom row) and 13 (center). Hence, multi-MHz OCT imaging offers a completely new averaging option: For speckle reduction, several complete 3D data sets can be acquired successively and then averaged ensuring that the same point in the sample is sampled at a sufficiently low repetition rate. The effect is expected to be similar to the shown frame averages taken at lower frame rates. Alternatively, a 3D cube with very high aspect ratio can be acquired which consists of merely a few B-frames slightly separated along the slow axis. These B-frames can be averaged for speckle reduction as shown in Fig. 13 (right). Shot noise and acquisition noise can be suppressed by any of the presented averaging methods. We find that for best image quality, the optimum number of averaged acquisitions is 5-8.

4. Conclusion and outlook

In conclusion, we present OCT imaging with good image quality at up to 20 million lines per second. A sustained net voxel rate of 4.5GVoxels per second is achieved over a 950 x 640 x 360 volume. Such a 3D data set is acquired within 25ms. 4.5GVoxels per second, 14,600 frames per second and a volume acquisition time corresponding to 40 volumes per second represents the fastest sustained 2D and 3D OCT speed demonstrated so far measured by frame rate, line rate and voxel rate.

Several techniques to push the speed have been applied, and the related performance data, problems and advantages of laser, data acquisition system and optical layout are discussed in detail. This includes the design and implementation of an FDML laser with a 5MHz wavelength sweep repetition rate, the layout of an optical multi-spot beam delivery system with a greatly improved back-coupling efficiency, a novel algorithm for line de-interlacing from the bidirectional scans, and an algorithm for seamless fusion of the different 3D data volumes.

This work implies that in the future, multi-megahertz OCT systems with good image quality might be available for high definition 3D snapshots in a series of applications. This might dramatically improve the ease of use in clinical application with patients.

Further, especially for the extraction of phase information for Doppler imaging this high speed offers the great advantage that by comparing adjacent A-scans and simultaneously adjacent B-frames, a huge dynamic range of Doppler flow velocities could be measured.

Also, by simply averaging adjacent voxels from the stable speckle pattern of a 3D volume, the image quality can be improved in a much more defined way than by frame averaging with slower systems and relying on sample motion. Considering frame counts of 3-7 for effective speckle averaging, multi-megahertz OCT systems can provide high quality images at many 100kHz.

The reduction of the total scanning time combined with ultra-rapid translation of the spot on the sample might also enable increased optical powers on the sample because of the reduced total absorbed energy. It should be emphasized that for a single OCT volume acquisition, once the scan speed is fast enough to represent only a pulsed illumination for each spot on the sample, further increased OCT imaging speed at constant sensitivity might be possible since the amount of light (i.e. the amount of photons per scanned sample location) stays constant, so more power can be applied.

Acknowledgements

The authors acknowledge support from Prof. W. Zinth at the Ludwig-Maximilians-University Munich. This research was sponsored by the Emmy Noether Program of the German Research Foundation (DFG - HU 1006/2-1) and the European Union project FUN OCT FP7 HEALTH, contract no. 201880.

#126756 - $15.00 USD Received 9 Apr 2010; revised 4 Jun 2010; accepted 15 Jun 2010; published 30 Jun 2010
(C) 2010 OSA